# Fracture induced anisotropy in poroelastic media. A finite element approach.

## Juan E. Santos

Department of Mathematics, **Purdue University** and

Instituto del Gas y del Petróleo, **Facultad de Ingeniería UBA** and

Universidad Nacional de La Plata **(UNLP)**

Work in collaboration with J.M. Carcione **(OGS)**, P. M. Gauzellino **(UNLP)**

and R. Martínez Corredor **(UNLP)**

**Department of Mathematics, Purdue University, Bridge to Research, 2/9/2016**

# Introduction. I

- A planar fracture embedded in a fluid-saturated poroelastic – Biot - medium can be modeled as a extremely thin, highly permeable and compliant porous layer.

- A Biot medium containing a dense set of aligned fractures behaves as an effective transversely isotropic and viscoelastic **(TIV)** medium when the average fracture distance is much smaller than the predominant wavelength of the traveling waves.

- This leads to frequency and angular variations of velocity and attenuation of seismic waves.

# Introduction. II

- **P-waves traveling in this type of medium induce fluid-pressure gradients at fractures and mesoscopic-scale heterogeneities, generating fluid flow and slow (diffusion) Biot waves, causing attenuation and dispersion of the fast modes (mesoscopic loss).**

- **A poroelastic medium with embedded aligned fractures exhibits significant attenuation and dispersion effects due to this mechanism.**

- **Due to the extremely fine meshes needed to properly represent these mesoscopic-scale fractures, numerical simulations are very expensive or even not feasible.**

# Introduction. III

- **Our approach:** In the context of **Numerical Rock Physics**, we use a **numerical upscaling procedure** to determine the complex and frequency dependent stiffness at the macroscale of a TIV medium equivalent to a Biot medium with aligned fractures.

- To determine the **complex stiffness** coefficients of the **equivalent TIV medium at the macroscale**, we solve a set of boundary value problems (BVP's) for Biot's equation in the diffusive range.

- The BVP's are stated and solved in the space-frequency-domain using the finite-element method **(FEM).**

# Introduction. IV

- **The BVP's represent  harmonic tests at a finite number of frequencies on a representative sample of the material.**

- **Numerical Rock Physics offer an alternative to laboratory measurements.**

- **Numerical experiments are inexpensive and informative since the physical process of wave propagation can be inspected during the experiment.**

- **Moreover, they are  repeatable, essentially free from experimental errors, and may easily be run using alternative models of the rock and fluid properties.**

- For Biot's media, White et al. (1975) were the first to introduce the mesoscopic-loss mechanism in the framework of Biot's theory.

- For fine layered poroelastic materials, the theories of Gelinsky and Shapiro (GPY, 62, 1997) and Krzikalla and Müller (GPY, 76, 2011) allow to obtain the **five** complex and frequency-dependent stiffnesses of the **equivalent TIV medium**.

- To provide a more general modeling tool, we present a **numerical upscaling procedure** to obtain the complex stiffnesses of the effective **TIV** medium.

# The Mesoscale. Anisotropic poroelasticity. II

- **We employ the FEM to solve in the space-frequency domain Biot's equations in the diffusive range with boundary conditions representing compressibility and shear harmonic experiments.**

- **The methodology is applied to saturated isotropic poroelastic samples having a dense set of horizontal fractures.**

- **The samples contained mesoscopic-scale heterogeneities due to patchy brine-$CO_2$ saturation and fractal porosity and consequently, fractal permeability and frame properties.**

- **Applying a Bond transfomation matrix, the macroscale stiffness coefficients can be used to represent fractures at any orientation.**

**Let us consider isotropic fluid-saturated poroelastic layers.**

$\mathbf{u}^s(\mathbf{x}, \omega)), \mathbf{u}^f(\mathbf{x}, \omega))$ **: time Fourier transform of the displacement vector of the solid and fluid relative to the solid frame, respectively.**

$\omega = 2\pi f$ **: the angular frequency.**

$\mathbf{u}(\mathbf{x}, \omega)) = (\mathbf{u}^s(\mathbf{x}, \omega), \mathbf{u}^f(\mathbf{x}, \omega))$

$\sigma_{kl}(u), \mathbf{p}_f(u)$ **: time Fourier transform of the total stress and the fluid pressure, respectively**

**On each plane layer $n$ in a sequence of $N$ poroelastic layers, the frequency-domain stress-strain relations are**

$$\sigma_{kl}(u) = 2\mu\,\varepsilon_{kl}(u^s) + \delta_{kl}\left(\lambda_G\,\nabla \cdot u^s + \alpha M \nabla \cdot u^f\right),$$
$$\mathbf{p}_f(u) = -\alpha M \nabla \cdot u^s - M \nabla \cdot u^f.$$

# Elastic coefficients. I

$$\alpha = 1 - \frac{K_m}{K_s}, \quad M = \left[\frac{\alpha - \phi}{K_s} + \frac{\phi}{K_f}\right]^{-1},$$

$$K_G = K_m + \alpha^2 M, \quad \lambda_G = K_G - \frac{2}{3}\mu,$$

$K_G$: **Gassmann's (closed) bulk modulus of the saturated material.**

$\mu$: **shear modulus of the dry matrix**

$K_m$: **bulk modulus of the dry matrix**

$K_s$: **bulk modulus of the solid grains**

$K_f$: **bulk modulus of the saturant fluid**

$\phi$: **effective porosity**

**Biot's equations in the diffusive range:**

$$\nabla \cdot \sigma(u(x,\omega)) = 0,$$
$$i\omega \frac{\eta}{\kappa} u^f(x,\omega) + \nabla p_f(u(x,\omega)) = 0.$$

$\eta$: **fluid viscosity**    $\kappa$: **frame permeability**

# The TIV medium at the Macroscale.

$\tau_{ij}$: **stress tensor of the equivalent TIV medium**

**For a closed system( $\nabla \cdot u^f = 0$), the corresponding stress-strain**

**relations, stated in the space-frequency domain, are**

$$\tau_{11}(u) = p_{11}\, \epsilon_{11}(u^s) + p_{12}\, \epsilon_{22}(u^s) + p_{13}\, \epsilon_{33}(u^s),$$

$$\tau_{22}(u) = p_{12}\, \epsilon_{11}(u^s) + p_{11}\, \epsilon_{22}(u^s) + p_{13}\, \epsilon_{33}(u^s),$$

$$\tau_{33}(u) = p_{13}\, \epsilon_{11}(u^s) + p_{13}\, \epsilon_{22}(u^s) + p_{33}\, \epsilon_{33}(u^s),$$

$$\tau_{23}(u) = 2\, p_{55}\, \epsilon_{23}(u^s),$$

$$\tau_{13}(u) = 2\, p_{55}\, \epsilon_{13}(u^s),$$

$$\tau_{12}(u) = 2\, p_{66}\, \epsilon_{12}(u^s).$$

**This approach provides the complex velocities of the fast modes and**
**takes into account interlayer flow effects.**

**To determine the complex stiffness we solve Biot's equation in the 2D case on a reference square $\Omega = (0, L)^2$ with boundary $\Gamma$ in the $(x_1, x_3)$-plane. Set $\Gamma = \Gamma^L \cup \Gamma^B \cup \Gamma^R \cup \Gamma^T$, where**

$$\Gamma^L = \{(x_1, x_3) \in \Gamma : x_1 = 0\}, \quad \Gamma^R = \{(x_1, x_3) \in \Gamma : x_1 = L\},$$

$$\Gamma^B = \{(x_1, x_3) \in \Gamma : x_3 = 0\}, \quad \Gamma^T = \{(x_1, x_3) \in \Gamma : x_3 = L\}.$$

# The harmonic experiments to determine the stiffness coefficients. II

**The sample is subjected to  harmonic compressibility and shear tests described by the following sets of  boundary conditions.**

$p_{33(\omega)}$**:**

$$\sigma(u)\nu \cdot \nu = -\Delta P, \quad (x_1, x_3) \in \Gamma^T,$$

$$\sigma(u)\nu \cdot \chi = 0, \quad (x_1, x_3) \in \Gamma,$$

$$u^s \cdot \nu = 0, \quad (x_1, x_3) \in \Gamma^L \cup \Gamma^R \cup \Gamma^B,$$

$$u^f \cdot \nu = 0, \quad (x_1, x_3) \in \Gamma.$$

$\nu$**: the unit outer normal on** $\Gamma$

$\chi$**: a unit tangent on** $\Gamma$ **so that** $\{\nu, \chi\}$ **is an orthonormal system on** $\Gamma$**.**
**Denote by** $V$ **the original volume of the sample and by** $\Delta V(\omega)$ **its (complex) oscillatory volume change.**

**In the quasistatic case**

$$\frac{\Delta V(\omega)}{V} = -\frac{\Delta P}{p_{33}(\omega)},$$

**Then after computing the average $u_3^{s,T}(\omega)$ of the vertical displacements on $\Gamma^T$, we approximate**

$$\Delta V(\omega) \approx L u_3^{s,T}(\omega)$$

**which enable us to compute $p_{33}(\omega)$**

**To determine $p_{11}(\omega)$ we solve an identical boundary value problem than for $p_{33}$ but for a $90^{\text{o}}$ rotated sample.**

$p_{55}(\omega)$**: the boundary conditions are**

$$-\sigma(u)\nu = g, \quad (x_1, x_3) \in \Gamma^T \cup \Gamma^L \cup \Gamma^R,$$

$$u^s = 0, \quad (x_1, x_3) \in \Gamma^B,$$

$$u^f \cdot \nu = 0, \quad (x_1, x_3) \in \Gamma,$$

**where**

$$g = \begin{cases} (0, \Delta G), & (x_1, x_3) \in \Gamma^L, \\ (0, -\Delta G), & (x_1, x_3) \in \Gamma^R, \\ (-\Delta G, 0), & (x_1, x_3) \in \Gamma^T. \end{cases}$$

**The change in shape suffered by the sample is**

$$\tan[\theta(\omega)] = \frac{\Delta G}{p_{55}(\omega)}. \tag{1}$$

$\theta(\omega)$**: the angle between the original positions of the lateral boundaries and the location after applying the shear stresses.**

**Since**

$\tan[\theta(\omega)] \approx u_1^{s,T}(\omega)/L$**, where** $u_1^{s,T}(\omega)$ **is the average horizontal displacement at** $\Gamma^T$**,** $p_{55}(\omega)$ **can be determined from (1).**

**to determine** $p_{66}(\omega)$ **(shear waves traveling in the** $(x_1, x_2)$**-plane), we rotate the layered sample** $90^O$ **and apply the shear test as indicated for** $p_{55}(\omega)$**.**

$p_{13}(\omega)$**: the boundary conditions are**

$$\sigma(u)\nu \cdot \nu = -\Delta P, \quad (x_1, x_3) \in \Gamma^R \cup \Gamma^T,$$

$$\sigma(u)\nu \cdot \chi = 0, \quad (x_1, x_3) \in \Gamma,$$

$$u^s \cdot \nu = 0, \quad (x_1, x_3) \in \Gamma^L \cup \Gamma^B, \quad u^f \cdot \nu = 0, \quad (x_1, x_3) \in \Gamma.$$

**In this experiment** $\epsilon_{22} = \nabla \cdot u^f = 0$**, so that**

$$\tau_{11} = p_{11}\epsilon_{11} + p_{13}\epsilon_{33}, \quad \tau_{33} = p_{13}\epsilon_{11} + p_{33}\epsilon_{33}, \tag{2}$$

$\epsilon_{11}, \epsilon_{33}$**: the strain components at the right lateral side and top side of the sample, respectively. Then,**

$$p_{13}(\omega) = (p_{11}\epsilon_{11} - p_{33}\epsilon_{33}) / (\epsilon_{11} - \epsilon_{33}).$$
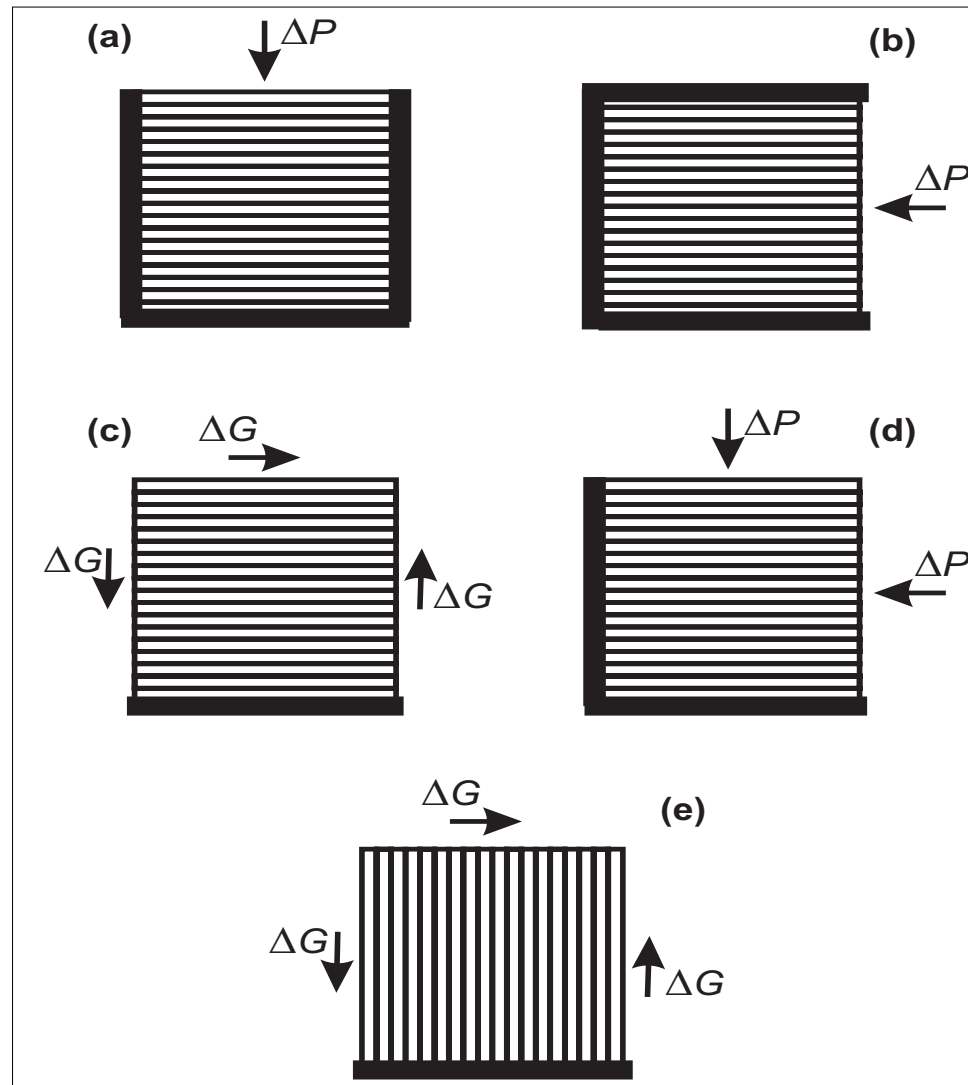
a): $p_{33}$,   b): $p_{11}$,   c): $p_{55}$,   d): $p_{13}$   e): $p_{66}$

**Solid dofs**

**Fluid (x-comp) dofs**

**Fluid (y-comp) dofs**

The solution of the oscillatory tests was computed using the **FEM**. The figure displays the local degrees of freedom **(DOFs)** associated with each component of the solid displacement and the fluid displacement vectors. The **apriori error estimate in the energy norm is on the order of** $h^{1/2}$. Once we computed the $p_{IJ}$ coefficients, we can determine the velocities and attenuation factors of the equivalent TIV medium.

**Complex velocities of the equivalent TIV anisotropic medium:**

$$v_{qP} = (2\bar{\rho})^{-1/2}\sqrt{p_{11}l_1^2 + p_{33}l_3^2 + p_{55} + A},$$

$$v_{qSV} = (2\bar{\rho})^{-1/2}\sqrt{p_{11}l_1^2 + p_{33}l_3^2 + p_{55} - A},$$

$$v_{SH} = \bar{\rho}^{-1/2}\sqrt{p_{66}l_1^2 + p_{55}l_3^2},$$

$$A = \sqrt{[(p_{11} - p_{55})l_1^2 + (p_{55} - p_{33})l_3^2]^2 + 4[(p_{13} + p_{55})l_1l_3]^2}.$$

$\bar{\rho} = \langle\rho\rangle$: **average bulk density,**

$l_1 = \sin\theta$, $l_3 = \cos\theta$ **are the directions cosines,** $\theta$ **is the propagation angle between the wavenumber vector and the** $x_3$**-symmetry axis and the three velocities correspond to the qP, qSV and SH waves, respectively.**

## Velocities and attenuation in TIV media. II

**The seismic phase velocity and quality factors are:**

$$v_p = \left[ \mathrm{Re} \left( \frac{1}{v} \right) \right]^{-1} \quad \text{and} \quad Q = \frac{\mathrm{Re}(v^2)}{\mathrm{Im}(v^2)},$$

**where $v$ represents either $v_{\mathrm{qP}}$, $v_{\mathrm{qSV}}$ or $v_{\mathrm{SH}}$.**

**The energy-velocity vector $\mathbf{v}_e$ of the qP and qSV waves is**

$$\frac{\mathbf{v}_e}{v_p} = (l_1 + l_3 \cot \psi)^{-1} \hat{\mathbf{e}}_1 + (l_1 \tan \psi + l_3)^{-1} \hat{\mathbf{e}}_3,$$

**$\psi$: angle between the energy-velocity vector and the $x_3$-axis.**

**The energy velocity of the SH wave is**

$$\mathbf{v}_e = \frac{1}{\bar{\rho} v_p} \left( l_1 p_{66} \hat{\mathbf{e}}_1 + l_3 p_{55} \hat{\mathbf{e}}_3 \right).$$

A set of numerical examples consider the following cases for a square poroelastic sample of 160 cm side length and 10 periods of 1 cm fracture, 15 cm background.

Discretization: 160x160 uniform mesh, mesh size 1 cm:

- Case 1: A brine-saturated sample with fractures.

- Case 2: A brine-$CO_2$ patchy saturated sample without fractures.

- Case 3: A brine-$CO_2$ patchy saturated sample with fractures.

- Case 4: A brine saturated sample with a fractal frame and fractures.

The discrete boundary value problems to determine the complex stiffnesses $p_{IJ}(\omega)$ were solved for 30 frequencies using a public domain sparse matrix solver package.

The $p_{IJ}(\omega)$'s determine in turn the energy velocities and dissipation coefficients shown in the next figures.

qP Waves

Velocity anisotropy caused by the fractures in cases 1 and 3 is enhanced for the case of patchy saturation, with

lower velocities when patches are present. The velocity behaves isotropically in case 2.

**qP Waves**



Legend:
- 1. Brine saturated medium with fractures
- 2. Patchy saturated medium without fractures
- 3. Patchy saturated medium with fractures

Axis label (vertical): **1000/Q (Z)**
Axis label (horizontal): **1000/Q (X)**
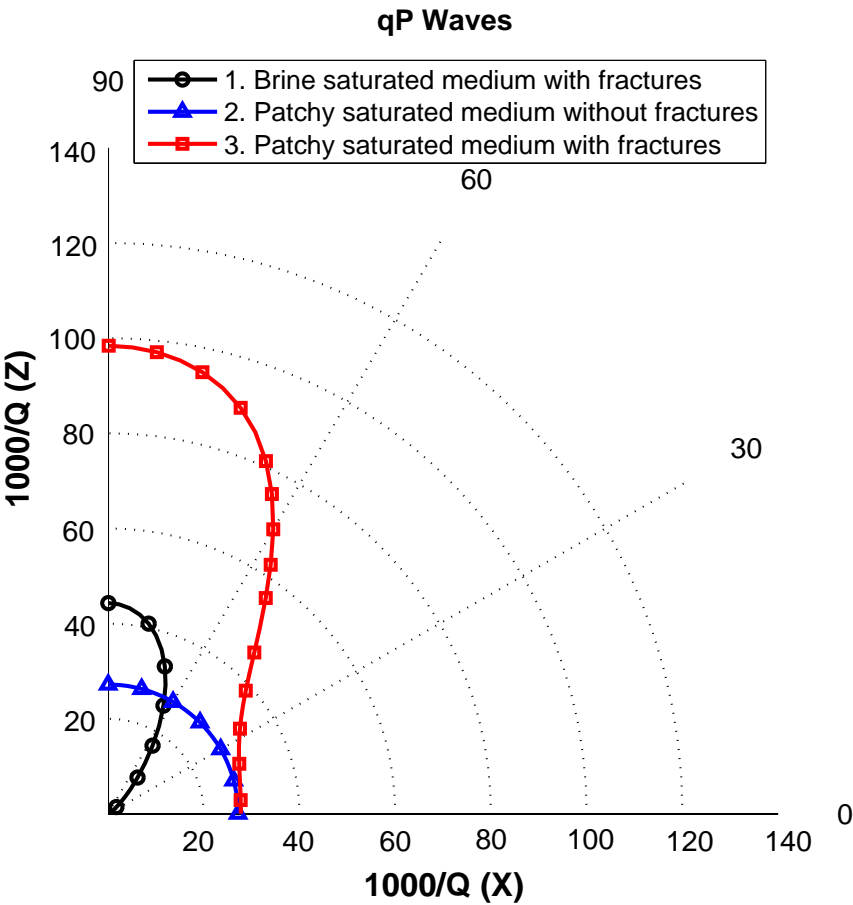
**Fractures induce strong Q anisotropy for angles normal to the fracture plane, enhanced by patchy saturation.**
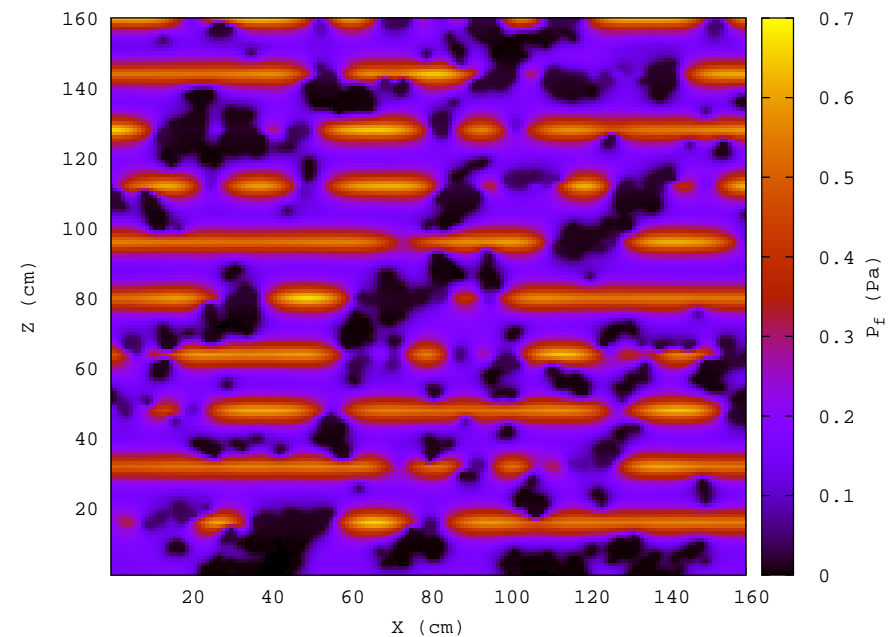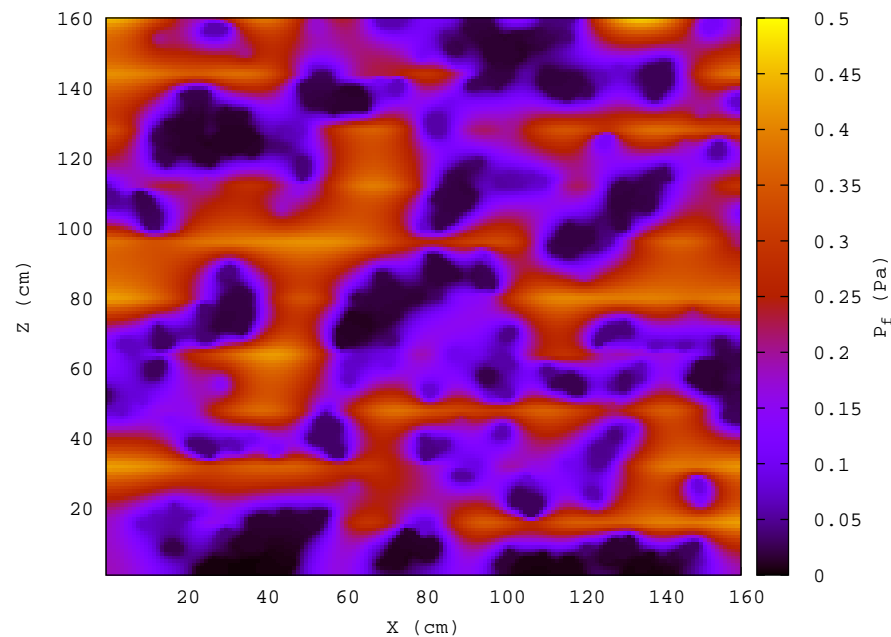
**Compression is normal to the fracture plane. Attenuation is stronger at 300 Hz.**

qSV Waves

- 1. Brine saturated medium with fractures
- 2. Patchy saturated medium without fractures
- 3. Patchy saturated medium with fractures

**Velocity anisotropy is induced by fractures (cases 1 and 3 ). Patchy saturation does not affect the anisotropic behavior of the qSV velocities. Case 2 shows isotropic velocity, with higher velocity values than for the fractured cases.**

**qSV Waves**
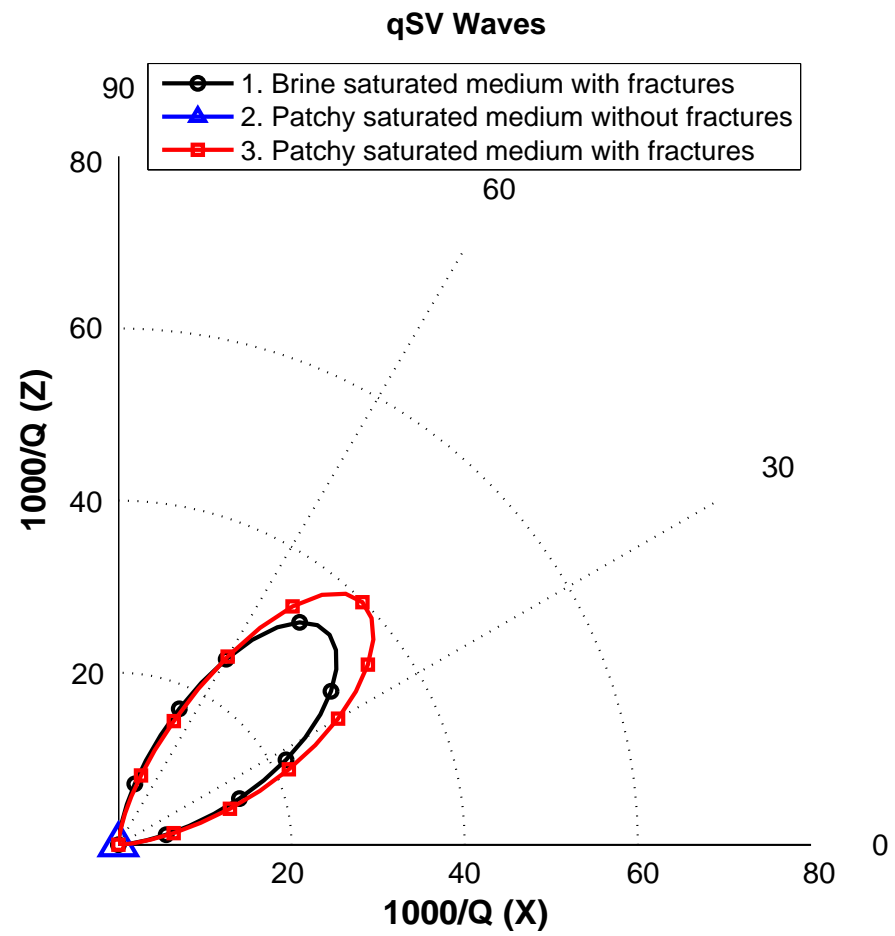
**qSV anisotropy is strong for angles between 30 and 60 degrees. The lossless case 2 is represented by a**

**triangle at the origin.**

**SH Waves**



- 1. Brine saturated medium with fractures
- 2. Patchy saturated medium without fractures
- 3. Patchy saturated medium with fractures

**SH velocity anisotropy is observed to be induced by fractures. Cases 1 and 3 are almost indistinguishable.**

**Velocity for case 2 is isotropic. SH waves are lossles, since $p_{55}$ and $p_{66}$ are real.**
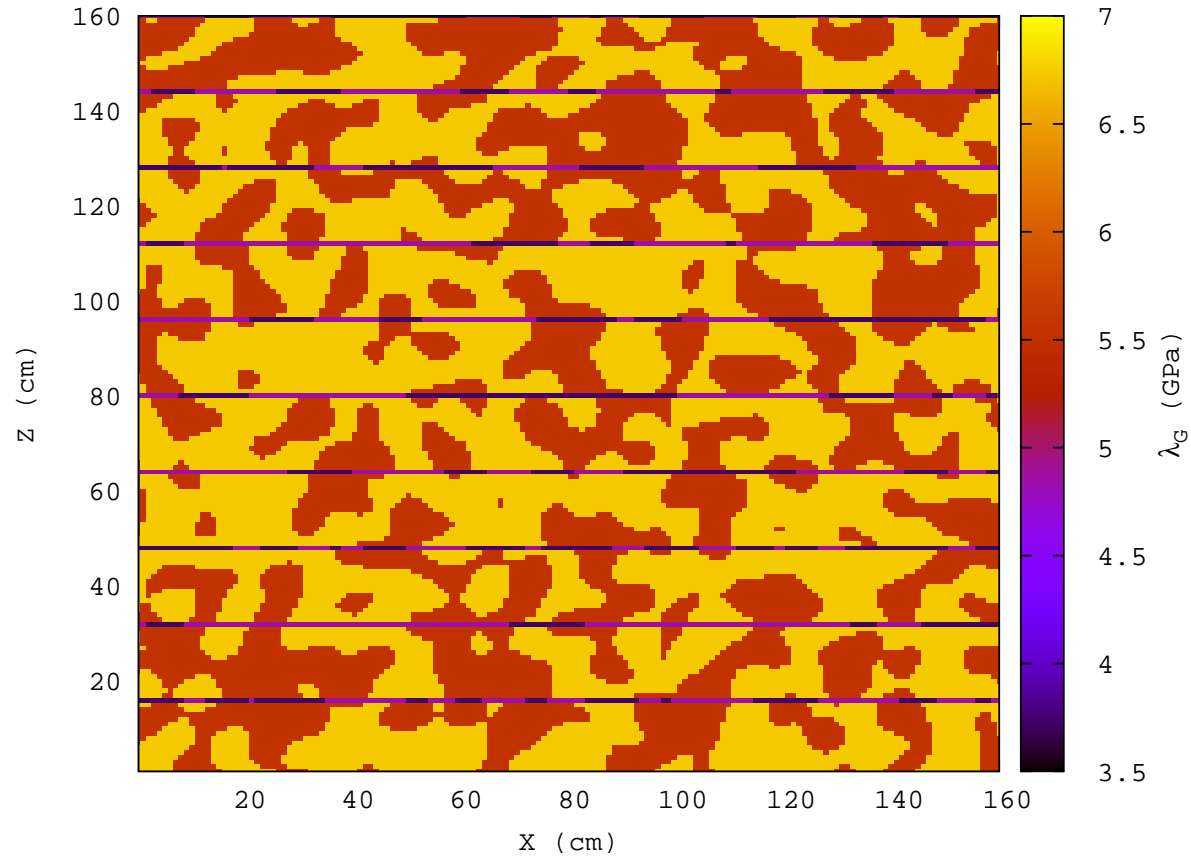
$$\log \kappa(x, z) = \langle \log \kappa \rangle + f(x, z), f(x, z)\text{: \textbf{fractal representing the spatial fluctuation of the permeability field}}$$

$\kappa(x, z)$.

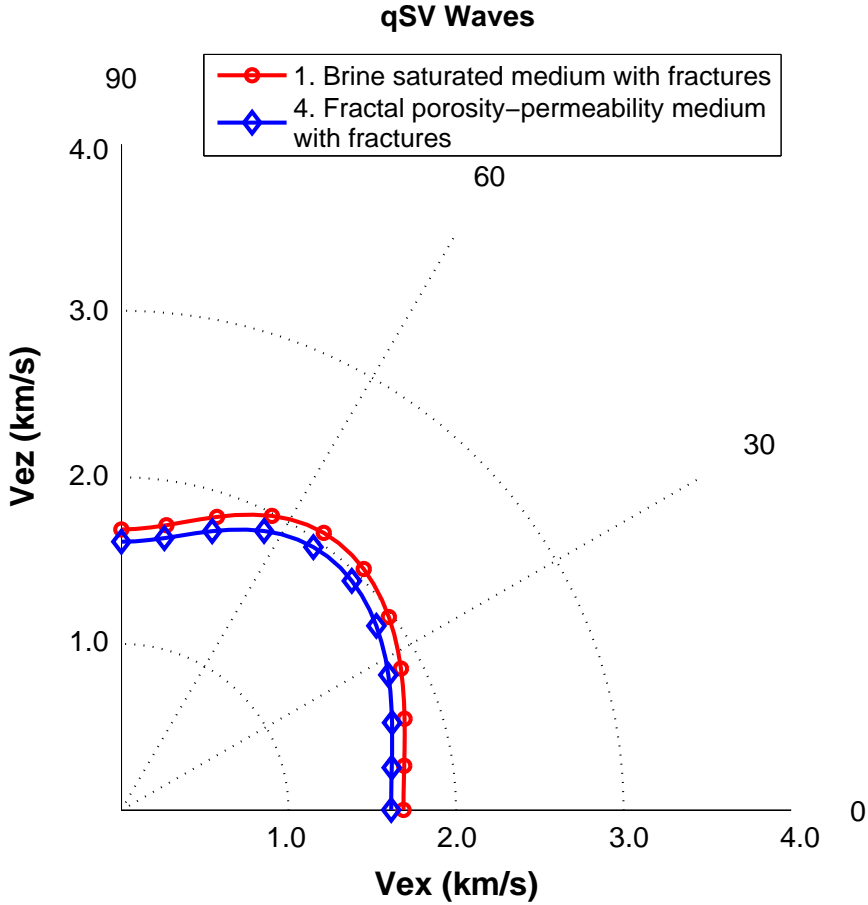**Polar representation of the qP energy velocity vector at 50 Hz for cases 1 and 4.**



qP Waves

Note the increase in Q anisotropy for qP waves for angles normal to the fracture plane.

**qP Waves**

Legend:
- 1. Brine saturated medium with fractures
- 4. Fractal porosity–permeability medium with fractures

Axis labels: **1000/Q (Z)**, **1000/Q (X)**

**Note the increase in Q anisotropy for qP waves for angles normal to the fracture plane.**

**Note the (small) increase in Q anisotropy for qSV waves for angles between 30 and 60 degrees.**

qSV Waves

1. Brine saturated medium with fractures
4. Fractal porosity–permeability medium with fractures
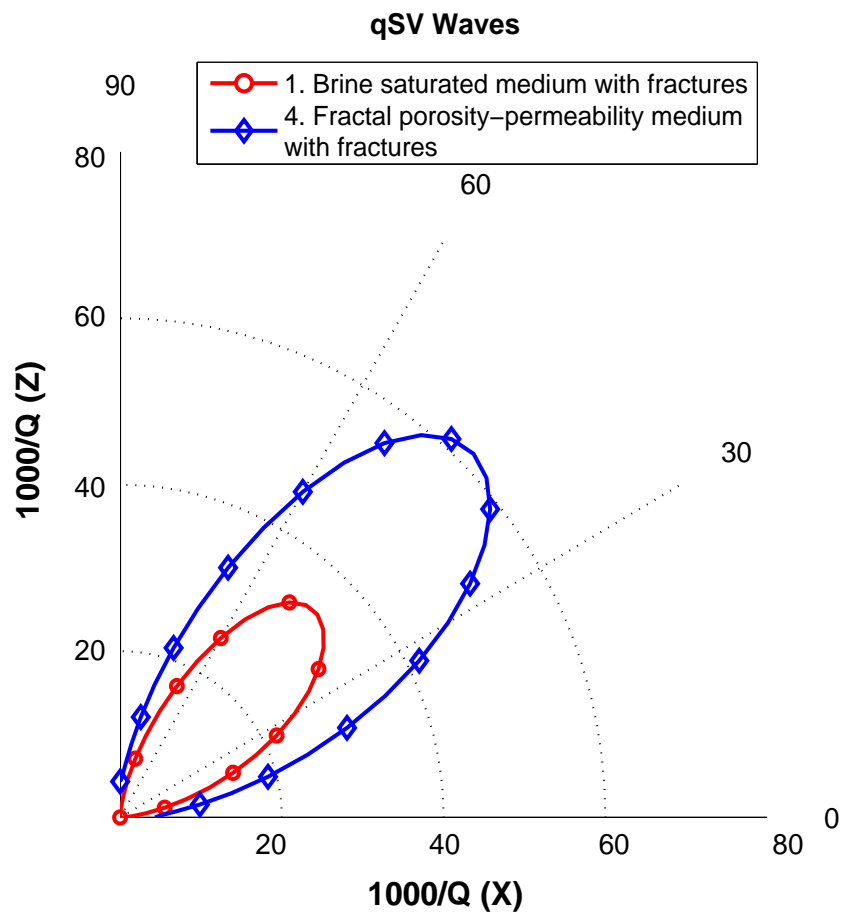
**Note a strong increase in Q anisotropy for angles between 30 and 60 degrees**

# The Macroscale I. Seismic modeling. Variational formulation

**We solve the following boundary value problem at the macroscale in a domain $\Omega$ with boundary $\partial\Omega$:**

$$-\omega^2 \rho u - \nabla \cdot \tau(u) = F, \quad \Omega$$

$$-\tau(u)\nu = i\omega \mathcal{D} u, \quad \partial\Omega, \textbf{(absorbing bounday condition, } D > 0\textbf{)}$$

$u = (u_x, u_z)$**: displacement vector,** $\rho$**: average density.**

$\tau(u)$**: stress-tensor of our equivalent TIV medium, defined in terms of the** $p'_{IJ}s$**.**

**A global continuous variational formulation: Find** $u(x, \omega) \in [H^1(\Omega)]^2$ **such that**

$$-(\rho\omega^2 u, \varphi) + (\tau(u), \varepsilon(\varphi)) + i\omega \langle \mathcal{D}u, \varphi \rangle_{\partial\Omega} = (f, \varphi), \quad \varphi \in [H^1(\Omega)]^2,$$

# The Macroscale. II. Global continuous and FE variational formulation.

$\mathcal{T}^h$: **a partition of** $\bar{\Omega}$ **into rectangles of diameter bounded by** $h$:

$$\bar{\Omega} = \cup_{j=1}^{J} \Omega_j$$

$\Gamma_j = \partial\Omega \cap \partial\Omega_j$, $\Gamma_{jk} = \Gamma_{kj} = \partial\Omega_j \cap \partial\Omega_k$; $\xi_{jk}$ **the centroids of** $\Gamma_j$ **and** $\Gamma_{jk}$.

**Reference rectangular element**

$$R = [-1, 1]^2, \qquad S(R) = \mathrm{Span} \left\{ 1, x, z, \left( x^2 - \frac{5}{3}x^4 \right) - \left( z^2 - \frac{5}{3}z^4 \right) \right\}.$$

**The DOF associated with** $S$: **values at the mid points of the faces of** $R$.

**If** $a_1 = (-1, 0)$, $a_2 = (0, -1)$, $a_3 = (1, 0)$ **and** $a_4 = (0, 1)$,

**the basis function**

$\psi_1(x, z) = \frac{1}{4} - \frac{1}{2}x - \frac{3}{8}\left[ (x^2 - \frac{5}{3}x^4) - (z^2 - \frac{5}{3}z^4) \right]$

**is such that**

$\psi_1(a_1) = 1$ **and** $\psi_1(a_j) = 0$, $j = 2, 3, 4$.

# The Macroscale. III. Global FE variational formulation.

**The nonconforming FE space** $\mathcal{NC}^h$

$$\mathcal{NC}^h = \{\varphi \in [L^2(\Omega)]^2 : \varphi_j \in [S(\Omega_j)]^2, \quad \varphi_j(\xi_{jk}) = \varphi_k(\xi_{jk}) \forall j, k\},$$

$\varphi_j$**: the restriction of** $\varphi$ **as seen from** $\Omega_j$**. The global nonconforming FE procedure: Find** $u^h \in \mathcal{NC}^h$ **such that**

$$-(\rho\omega^2 u^h, \varphi) + \sum_j (\tau(u^h), \varepsilon(\varphi))_{\Omega_j} + \mathrm{i}\omega \langle \mathcal{D}u^h, \varphi \rangle_{\partial\Omega} = (f, \varphi), \quad \varphi \in \mathcal{NC}^h.$$

**Instead of solving the global algebraic problem associated with the global FE procedure above, we will employ the iterative domain decomposition procedure.**

**Thus we avoid having to solve a global system of equations associated with a noncoercive Helmholtz-type problem.**

# The Macroscale. IV. FE Domain decomposition.

Consider the decomposed problem over $\Omega_j$ satisfying he interface consistency conditions

$$\tau_{jk}\nu_{jk} + i\beta_{jk}u_j = -\tau_{kj}\nu_{kj} + i\beta_{jk}u_k, \qquad x \in \Gamma_{jk} \subset \partial\Omega_j,$$

$$\tau_{kj}\nu_{kj} + i\beta_{jk}u_k = -\tau_{jk}\nu_{jk} + i\beta_{jk}u_j, \qquad x \in \Gamma_{kj} \subset \partial\Omega_k,$$

$\beta_{jk}$: **positive definite iteration matrix functions defined on the interior boundaries $\Gamma_{jk}$.**

To localize the calculations, we introduce a set of Lagrange multipliers $\lambda_{jk}^h$: associated with the stress values $-\tau(u_j)\nu_{jk}(\xi_{jk})$:

$$\widetilde{\Lambda}^h = \{\lambda^h \colon \lambda^h|_{\Gamma_{jk}} = \lambda_{jk}^h \in [P_0(\Gamma_{jk})]^2 = [\Lambda_{jk}^h]^2\}.$$

$P_0(\Gamma_{jk})$ **are constant functions on** $\Gamma_{jk}$**. Note that** $\Lambda_{jk}^h$ **and** $\Lambda_{kj}^h$ **are considered to be distinct.**

**Given an initial guess** $\left(\widehat{u}_j^{h,0}, \lambda_{jk}^{h,0}, \lambda_{kj}^{h,0}\right) \in [NC_j^h]^2 \times [\Lambda_{jk}^h]^2 \times [\Lambda_{kj}^h]^2$,

**compute** $\left(\widehat{u}_j^{h,n}, \lambda_{jk}^{h,n}\right) \in [NC_j^h]^2 \times [\Lambda_{jk}^h]^2$ **as the solution of the equations**

$$-(\rho\omega^2\widehat{u}_j^{h,n}, \varphi)_j + \sum_{pq}(\tau_{pq}(\widehat{u}^{h,n}), \varepsilon_{pq}(\varphi))_j + i\omega\left\langle\left\langle \mathcal{D}\widehat{u}_j^{h,n}, \varphi\right\rangle\right\rangle_{\Gamma_j}$$

$$+\sum_k\left\langle\left\langle \lambda_{jk}^{h,n}, \varphi\right\rangle\right\rangle_{\Gamma_{jk}} = (\widehat{f}, \varphi)_j, \quad \varphi \in [NC_j^h]^N,$$

$$\lambda_{jk}^{h,n} = -\lambda_{kj}^{h,n-1} + i\beta_{jk}[\widehat{u}_j^{h,n}(\xi_{jk}) - \widehat{u}_k^{h,n-1}(\xi_{jk})], \quad \textbf{on } \Gamma_{jk}.$$

It can be shown that if $u^h$ is the solution of the global FE procedure,

$$\|\widehat{u}^{h,n} - u^h\|_0 \to 0 \text{ in } [L^2(\Omega)]^2 \quad \text{when} \quad n \to \infty,$$

# The Macroscale Model. I

- **The macroscopic model consists of an isotropic square background $\Omega$ of 1.6 km side length containing an anisotropic layer of 400m thickness of either horizontal or vertical aligned fractures (HTI or VTI medium).**

- **The stiffnesses coefficients of the anisotropic layer are those determined using the harmonic experiments, for the cases of fully brine saturated fractures (Case 1) or 10 % patchy $CO_2$ saturation (Case 3).**

- **The isotropic background has P- and S-wave velocities at 50 Hz equal to 2633 m/s and 1270 m/s, respectively.**

# The Macroscale MOdel. II

- **For the HTI-case, qP- and qSV-wave velocities at 50 Hz are equal to 3808. m/s and 1686 m/s, respectively, while for the VTI-case qP- and qSV-wave velocities at 50 Hz are equal to 3008. m/s and 1686 m/s, respectively**

- **The computational mesh consists of square cells having side length 4 m, and The source is a dilatational perturbation of central frequency is 50 Hz, located at $(x = 800m, z = 6.m)$.**
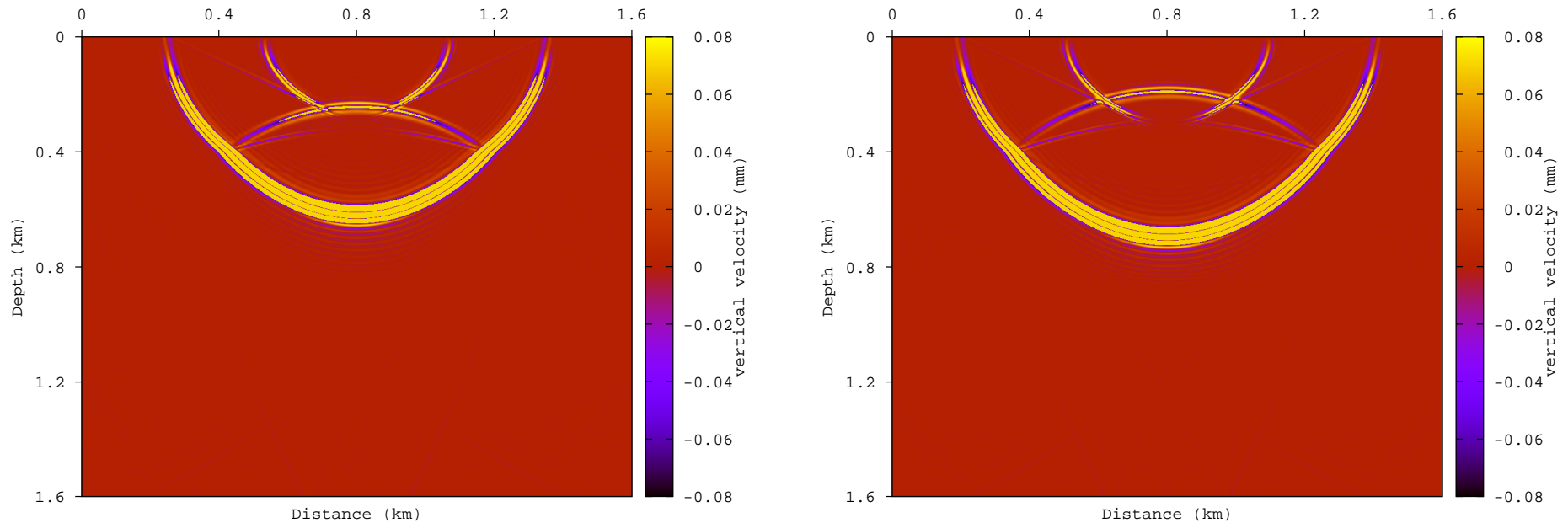
# The macroscopic model. III
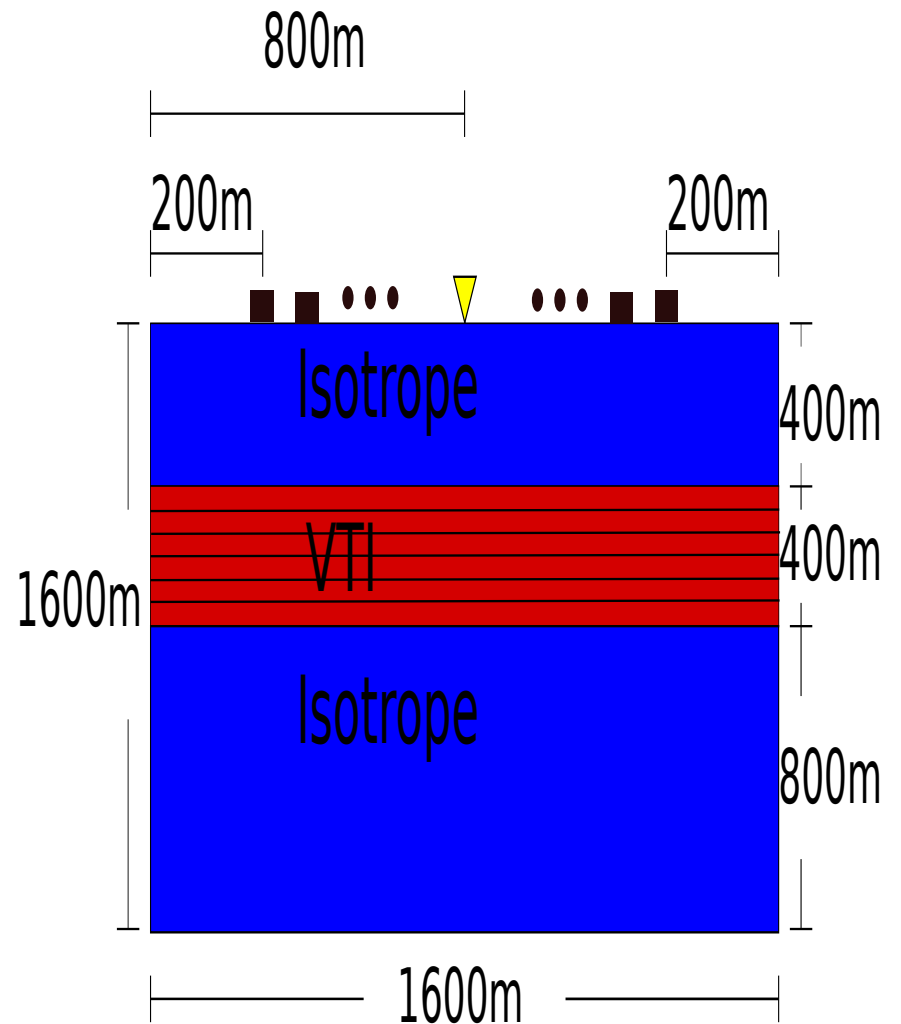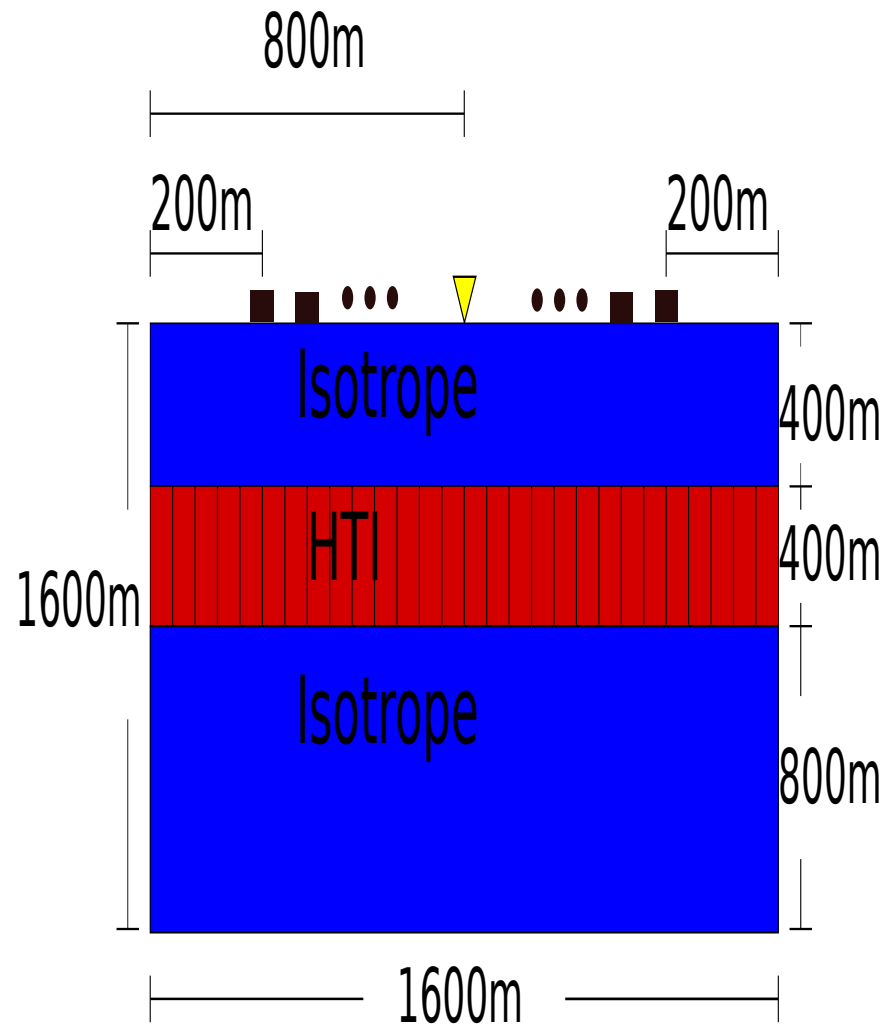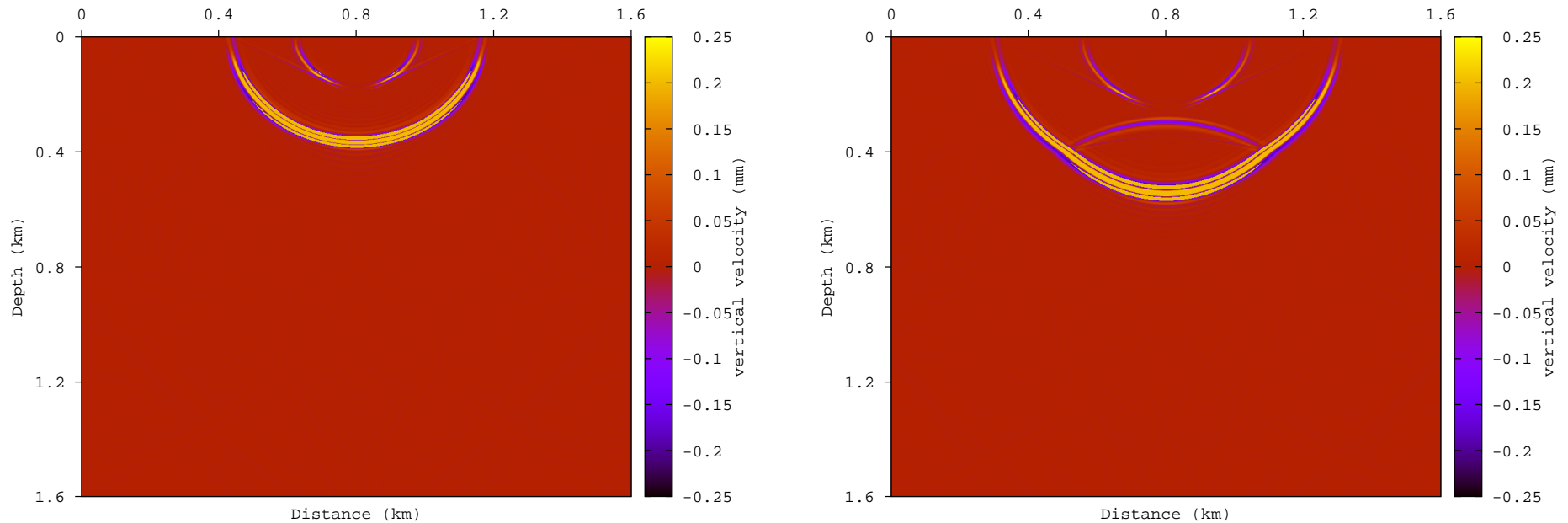
At 150 ms the incident P-wave is arriving to the top of the HTI layer. At 200 ms a reflected P-wave travelling upwards and a transmitted qP-wave travelling downwards are observed. The other wavefronts are S-waves generated by the point source at the top boundary.

**At 220 ms and 240 ms a reflected P-wave and travelling upwards and a transmitted qP-wave travelling downwards are observed. Note the deformation of the qP-wavefront because of the anisotropy in the HTI layer. The other (thin) wavefronts are S-waves generated by the point source at the top boundary.**

# Snapshots of z-component of velocity at 280ms (left) and 300 ms (right). HTI brine saturated fractures.
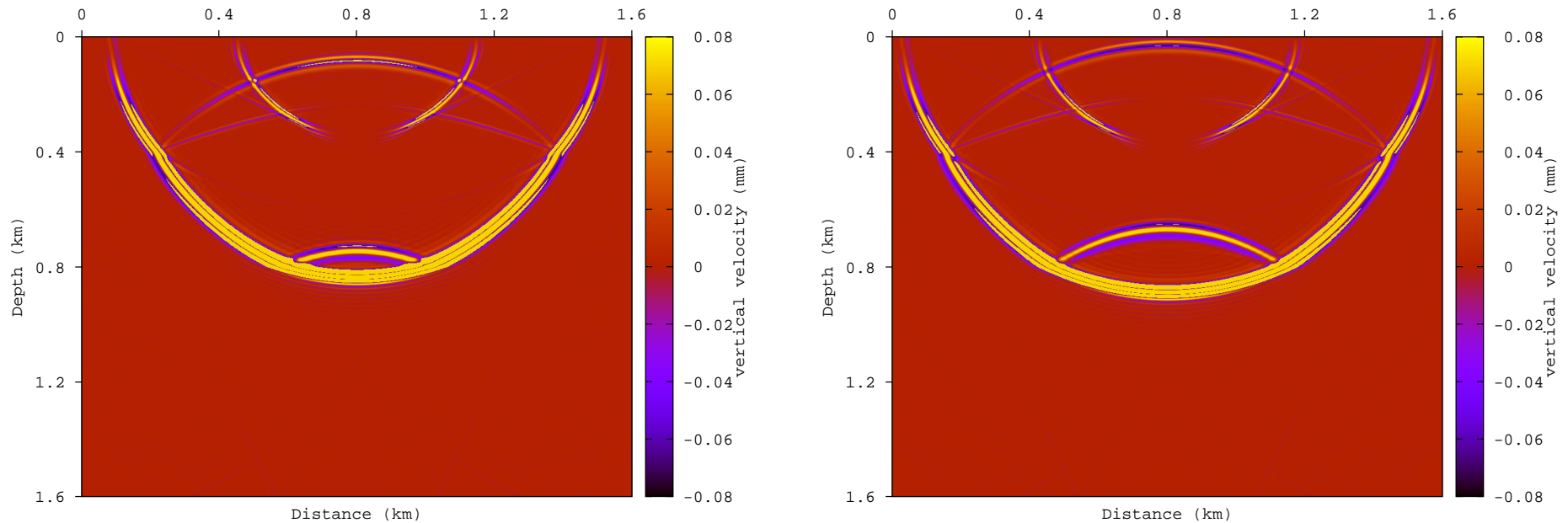


At 280 and 300 ms we can observe an upgoing P-wavefront and a tiny upgoing S-wavefront reflected at the top of the HTI layer and an upgoing qP-wavefront generated by reflection of the downgoing qP-wave at the bottom of the HTI layer. At 300 ms the reflected P-wave generated at the top of the HTI layer is arriving at the surface geophones.

# Snapshots of z-component of velocity at 380ms (left) and 500 ms (right). HTI brine saturated fractures.
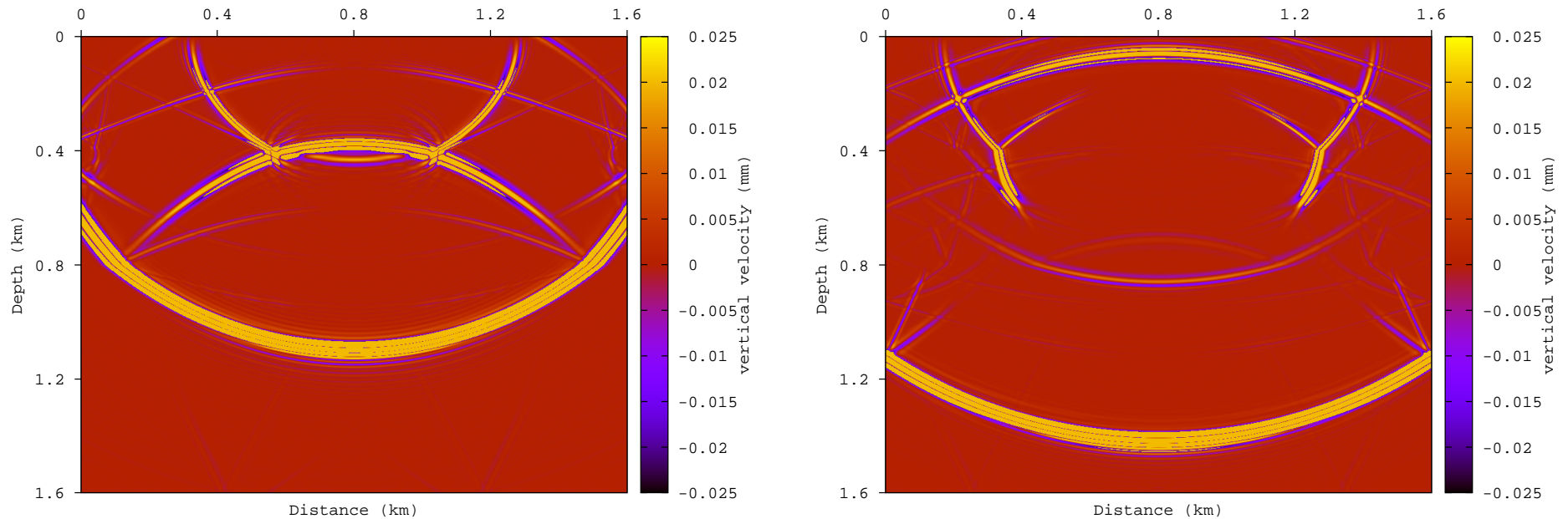


At 380 and 500 ms we can observe the reflected S-wave arriving at at the surface geophones, together with the qP-P wave reflected at the bottom of the HTI layer. The transmitted qP wave has already left the HTI layer and continues travelling downwards as a converted P-wave. Conversions to S-waves can also be seen in both snapshots
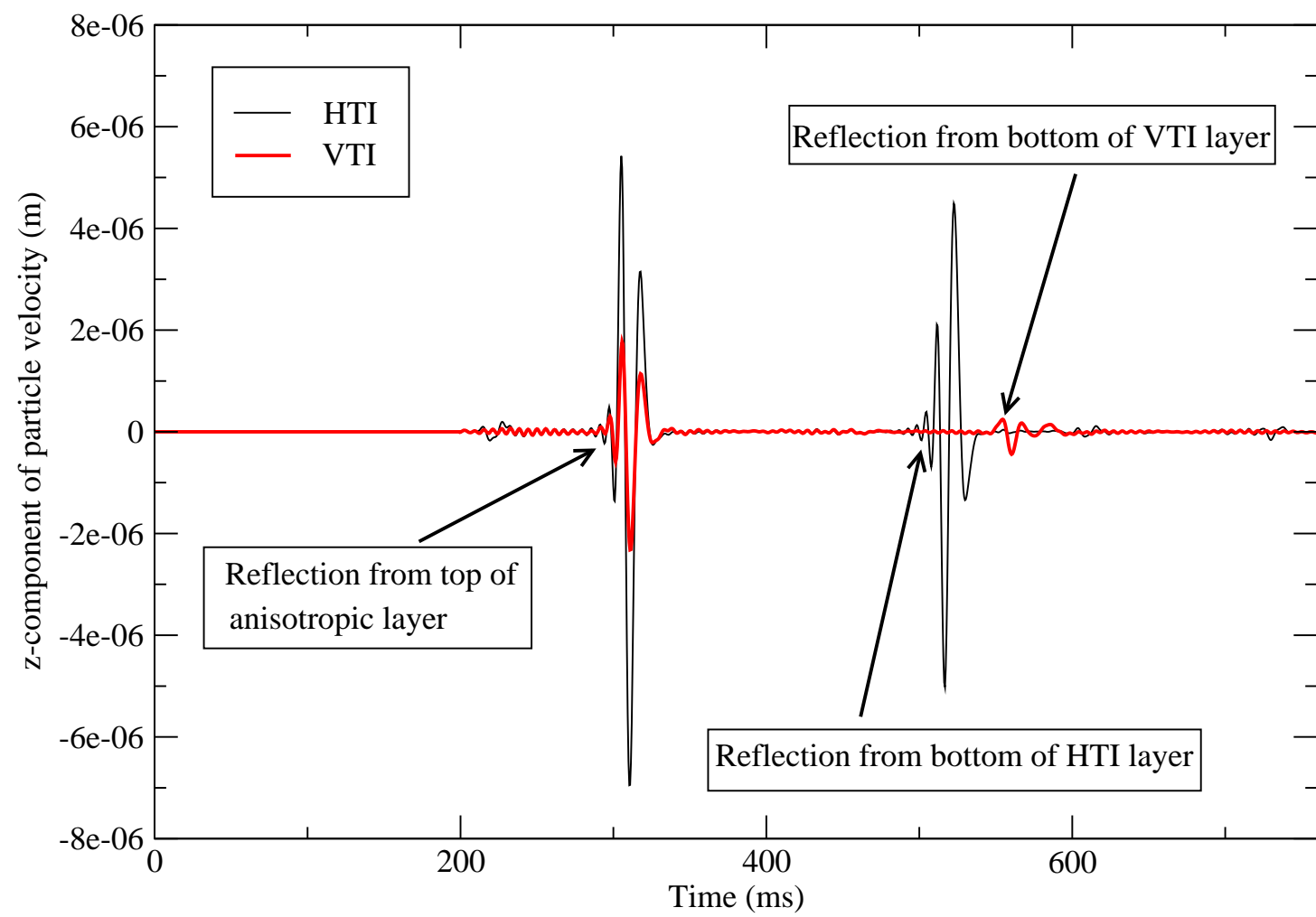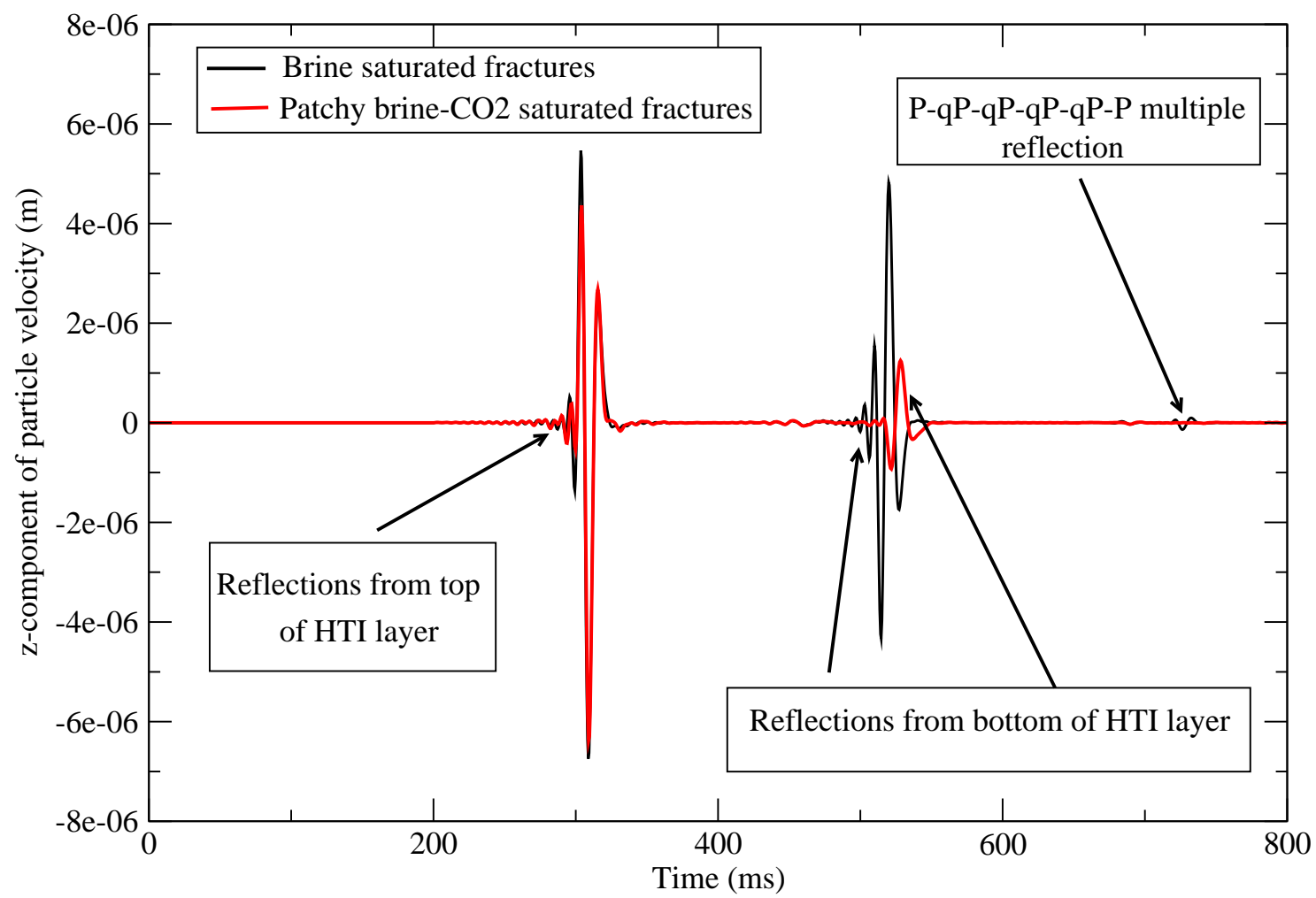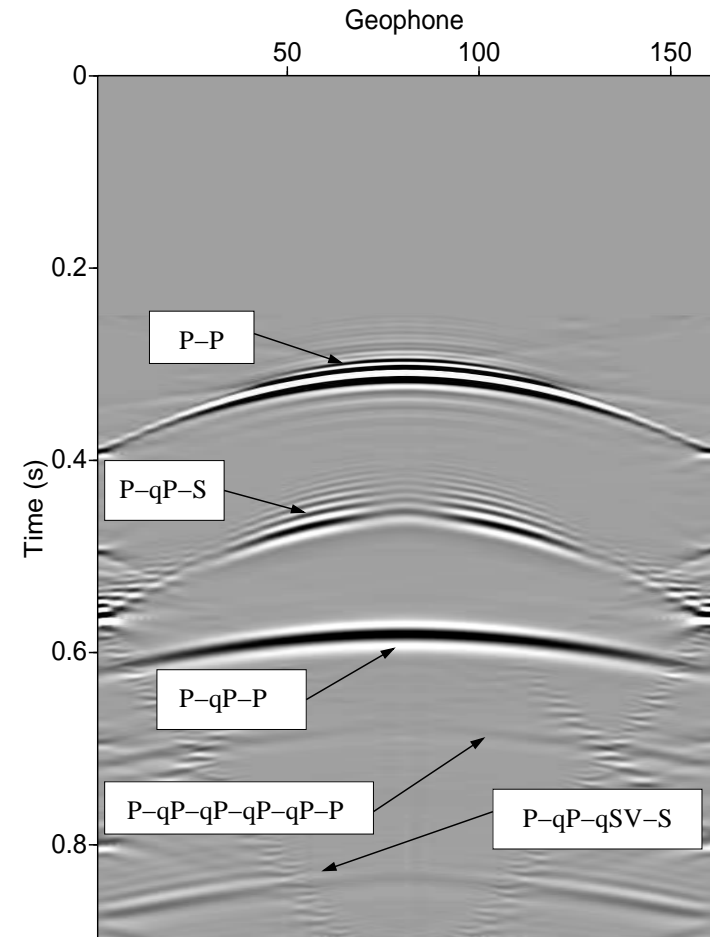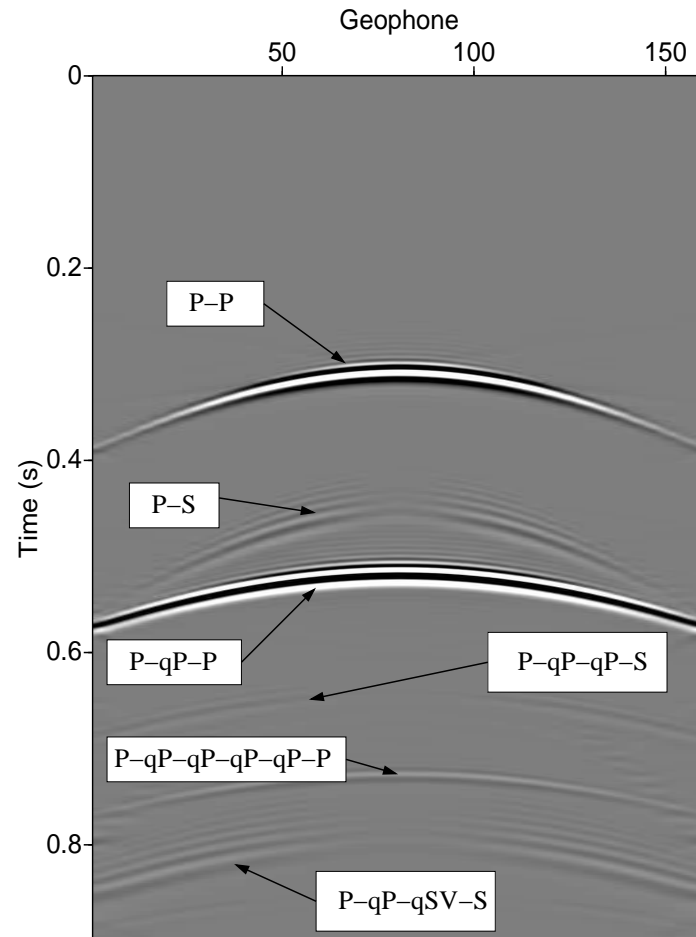
## Synthetic seismograms. HTI (left) and VTI (right) brine saturated fractures.



The seismograms show the arrivals of P and S waves reflected at the top of the HTI and VTI layers, as well as later arrivals corresponding to conversions from incident P to qP and qSV waves at the top and bottom of the layers. In particular, it is clearly seen the late **P-qP-P arrival** of the VTI case as compared with the corresponding one in the HTI case. The qP-velocities in the HTI and VTI layers are about 3800 m/s and 3000m/s, respectively.

# Synthetic seismograms. HTI brine (left) and 10 % $CO_2$ (right) saturated fractures.
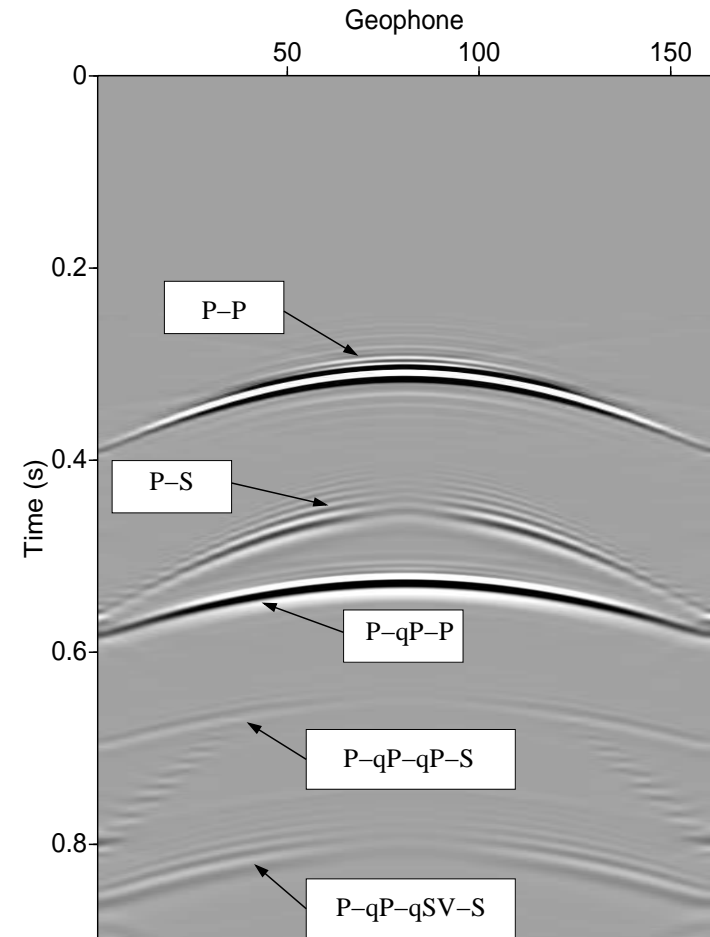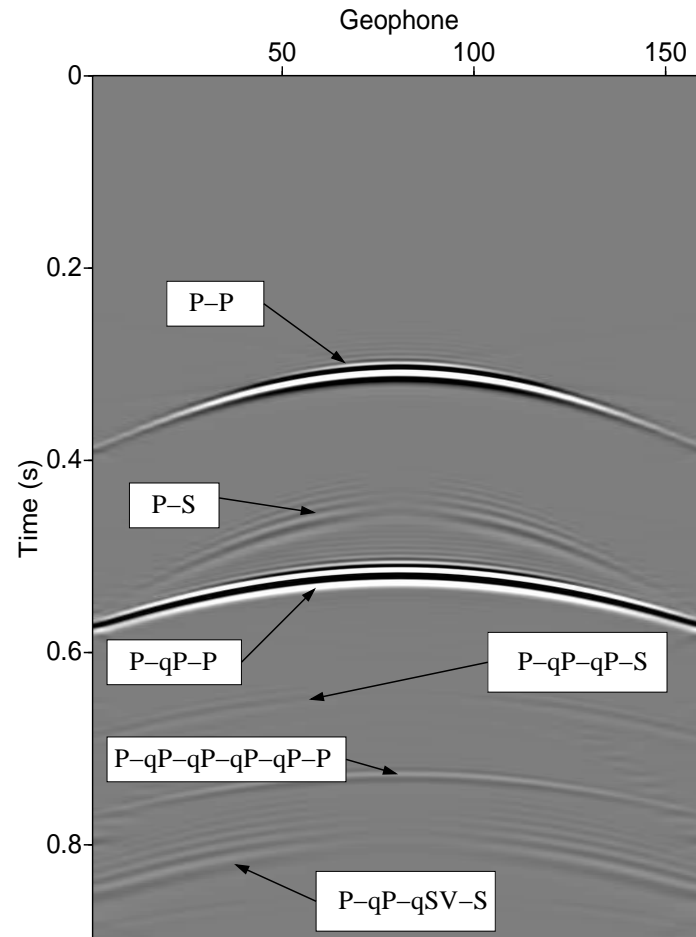


The seismograms show the arrivals of P and S waves reflected at the top of the HTI layer, and later arrivals corresponding to conversions from incident P to qP and qSV waves at the top and bottom of the layer. In particular, the **P-qP-qP-qP-qP-qP-P arrival** in the brine-saturated case is not seen in the patchy brine-$CO_2$ case due to the strong attenuation of qP waves when $CO_2$ is present ($Qp \approx 10$ at normal incidence). Instead qSV-waves are less attenuated when $CO_2$ is present and the **P-qP-qSV-S-arrival** is still observed.

# Conclusions

- **Numerical upscaling procedures allow to represent poroelastic samples with a dense set of aligned fractures at the mesoscopic-scale saturated by different fluids, bringing the induced anisotropy at the macroscale.**

- **THE FEM is a useful tool to solve local problems at the mesoscale in the context of Numerical Rock Physics and global wave propagation problems at the macroscale.**

- **The techniques presented here to model acoustics of porous media in geophysics can be extended to other fields, like ultrasound testing of quality of foods, groundwater flow and contamination among others.**

- **Thanks for your attention !!!!!.**